

Fast Approximate Inference for Spatial Extreme Value Models

Meixi Chen^a, Reza Ramezan^a, Martin Lysy^{a,*}

^a*Department of Statistics and Actuarial Science, University of Waterloo, Canada*

Abstract

The generalized extreme value (GEV) distribution is a popular model for analyzing and forecasting extreme weather data. To increase prediction accuracy, spatial information is often pooled via a latent Gaussian process on the GEV parameters. Inference for such hierarchical GEV models is typically carried out using Markov chain Monte Carlo (MCMC) methods. However, MCMC can be prohibitively slow and computationally intensive when the number of latent variables is moderate to large. In this paper, we develop a fast Bayesian inference method for spatial GEV models based on the Laplace approximation. Through simulation studies, we compare the speed and accuracy of our method to both MCMC and a more sophisticated but less flexible Bayesian approximation. A case study in forecasting extreme wind speeds is presented.

Keywords: Generalized extreme value distribution; latent spatial Gaussian process; Laplace approximation; Bayesian inference.

1. Introduction

Statistical modelling of extreme weather data has important applications including efficient wind energy management and damage prevention for floods and hurricanes. Extreme value theory (EVT) provides the tools for analyzing such data, covering a wide range of applications from climatology (Casson & Coles, 1999; Fawcett & Walshaw, 2006; Blanchet & Davison, 2011) to insurance and finance (Embrechts et al., 1997; Gilli & K ellezi, 2006). Developed under the EVT assumptions, the generalized extreme value (GEV) distribution is commonly used for analyzing a sequence of maxima within non-overlapping time periods. Hence, the GEV distribution is also known as the block maxima model. Coles (2001) provided an overview of the properties and applications of the GEV distribution with an emphasis on the analysis of hydrological and meteorological data.

Weather extremes are distinguished from other types of extremes due to the potential presence of spatial patterns. To incorporate the additional spatial information such as longitude and latitude into the analysis, Bayesian hierarchical modelling is a natural approach. The work of Smith & Naylor (1987) was the first to show the advantages of Bayesian analysis over likelihood-based methods in some cases of extreme value modelling. Coles & Powell (1996) reviewed the early studies

*Corresponding author

Email address: mlysy@uwaterloo.ca (Martin Lysy)

of Bayesian models of extreme values, and discussed the use of Bayesian methods to pool spatial information when data are sparse in the spatial domain. Later, [Coles & Casson \(1998\)](#) presented a simulation study of hurricane wind speeds where each GEV parameter was linked to the spatial covariates via a linear combination of a regression function and a Gaussian process. [Cooley et al. \(2007\)](#) modelled precipitation extremes as conditionally independent given the parameters, which are subsequently assumed to follow spatial Gaussian processes. Adding a copula model in the data layer, [Sang & Gelfand \(2010\)](#) dropped the conditional independence assumption, while retaining the spatial Gaussian process layer for the parameters. [Reich & Shaby \(2012\)](#) extended the GEV model framework to max-stable processes, which are an infinite-dimensional generalization of the GEV model. [Davison et al. \(2012\)](#) provided a comprehensive review of Bayesian hierarchical models of spatial extremes, discussing their development in terms of methodology and theoretical framework. Among this class of models, our paper focuses on the GEV models with spatial Gaussian process parameters, which are abbreviated as GEV-GP models.

There have been numerous applications of the GEV-GP framework to modelling of weather extremes in different regions and countries (e.g., [Dyrddal et al., 2015](#); [Tye & Cooley, 2015](#); [García et al., 2018](#)). However, inference for these complex models can be extremely time-consuming. The computational complexity of likelihood evaluations for the latent Gaussian process scales as $\mathcal{O}(n^3)$, where n is the number of sites being studied. Therefore, computations for large-scale spatial analyses involving numerous sites can quickly become prohibitively expensive. Several approaches to address this are outlined in [Section 2](#). Furthermore, exacerbating the high cost of each likelihood evaluation is the fact that the n latent variables corresponding to each location cannot be analytically integrated out. Instead, Markov Chain Monte Carlo (MCMC) methods are often used in the context of Bayesian inference to sample from the joint space of latent variables and model parameters. MCMC has the desirable property of producing exact posterior distributions given sufficient computing time and resources. Hamiltonian Monte Carlo (HMC) and its variants (e.g. [Duane et al., 1987](#); [Neal, 2011](#); [Hoffman & Gelman, 2014](#)) are especially effective MCMC algorithms for continuous variables, for which off-the-shelf implementations (e.g., Stan: [Stan Development Team, 2019](#)) have made fast and accurate Bayesian inference widely accessible. However, HMC is known to struggle with complex hierarchical models ([Stan Development Team, 2019](#), [Section 22.7](#)). In practice, it might take hours or days before convergence, especially when the number of spatial random effects is large.

In this paper, we develop a Bayesian inference method based on the Laplace approximation as an alternative to MCMC. The Laplace approximation converts a (typically intractable) integration problem into an optimization problem which is much easier to solve. The integrated nested Laplace approximation (INLA) approach ([Rue et al., 2009, 2017](#)) is an extension of the Laplace approximation and is often more accurate. A number of recent studies of weather extremes have successfully employed the INLA methodology to model the underlying spatio-temporal process ([Opitz et al.,](#)

2018; Castro-Camilo et al., 2019, 2020). However, the INLA methodology can only be applied to a restricted class GP models. In particular, it cannot be applied to GEV-GP models with more than one parameter modelled by a latent GP process. In contrast, the Laplace approximation being less restrictive is applicable to GEV-GP models with both location and scale parameters modelled as spatial random effects.

The remainder of this paper is structured as follows. Section 2 discusses the details of the GEV-GP model and our Bayesian Laplace approximation. Section 3 presents a simulation study where our method achieves the same accuracy as the MCMC method but two orders of magnitude faster. We also show here that the GEV-GP model with two spatial random effect parameters, rather than one, adds substantial flexibility to capture complex spatial dependence structures. Section 4 presents a case study analyzing extreme wind speeds in tropical cyclones. Concluding remarks are offered in Section 5. Efficient implementations of our methods are provided in the R/C++ library `SpatialGEV`, available at <https://github.com/meixichen/SpatialGEV>.

2. Methodology

The GEV-GP model is a hierarchical model with a data layer and a spatial random effects layer. Let $\mathbf{x}_1, \dots, \mathbf{x}_n \in \mathbb{R}^2$ denote the geographical coordinates of n locations, and let y_{ik} denote the extreme value measurement k at location i , for $k = 1, \dots, n_i$. The data layer specifies that each observation y_{ik} has a GEV distribution, denoted by $y \sim \text{GEV}(a, b_o, s_o)$, whose CDF is given by

$$F(y | a, b_o, s_o) = \begin{cases} \exp \left\{ - \left(1 + s_o \frac{y-a}{b_o} \right)^{-\frac{1}{s_o}} \right\} & s_o \neq 0, \\ \exp \left\{ - \exp \left(-\frac{y-a}{b_o} \right) \right\} & s_o = 0, \end{cases} \quad (1)$$

where $a \in \mathbb{R}$, $b_o > 0$, and $s_o \in \mathbb{R}$ are location, scale, and shape parameters, respectively. The support of the GEV distribution depends on the parameter values: y is bounded below by $a - b_o/s_o$ when $s_o > 0$, bounded above by $a - b_o/s_o$ when $s_o < 0$, and unbounded when $s_o = 0$. To capture the spatial dependence in the data, we assume some or all of the GEV parameters in the data layer are spatially varying. Thus they are introduced as random effects in the model.

In this paper, we employ a mixed-effects modelling strategy, where the location parameter $a(\mathbf{x})$ and the scale parameter $b_o(\mathbf{x})$ are modelled as spatially varying random effects, and a common shape parameter s_o is shared across all locations. Indeed, exploratory analyses using both simulated and real data have shown that modelling all three GEV parameters as random effects suffers from high numerical instability, possibly due to parameter identifiability issues. Moreover, the shape parameter s_o is known to be particularly difficult to estimate (Schliep et al., 2010; Cooley & Sain, 2010). Due to the positive constraint on the scale parameter, we reparametrize it by $b(\mathbf{x}) = \log(b_o(\mathbf{x}))$. Furthermore, we assume there is no upper bound on the extreme observations such that the shape parameter s_o must be non-negative. For simplicity, we take s_o to be positive, and work with the unconstrained parameter $s = \log(s_o)$.

In real data analyses, the dependence structure among the three GEV parameters is unclear unless prior knowledge can be obtained from previous studies. We follow the work of Cooley et al. (2007) and use independent latent Gaussian processes for $a(\mathbf{x})$ and $b(\mathbf{x})$. A zero-mean Gaussian process $z(\mathbf{x}) \sim \mathcal{GP}(0, k(\mathbf{x}, \mathbf{x}'))$ is fully characterized by its kernel function $k(\mathbf{x}, \mathbf{x}') = \text{Cov}(z(\mathbf{x}), z(\mathbf{x}'))$, which captures the strength of the spatial correlation between locations. We choose the squared-exponential kernel given by

$$k(\mathbf{x}, \mathbf{x}' | \sigma^2, \lambda) = \sigma^2 \exp \left\{ -\frac{\sqrt{\sum_{r=1}^2 (x_r - x'_r)^2}}{\lambda} \right\}, \quad (2)$$

where σ^2 is the amplitude parameter and $\lambda > 0$ is the length-scale parameter. Thus, σ^2 and λ are hyperparameters of the model.

We assume that given the locations, the data follow independent GEV distributions each with their own parameters. The complete GEV-GP hierarchical model then becomes

$$\begin{aligned} y_{ik} | a(\mathbf{x}_i), b(\mathbf{x}_i), s &\stackrel{\text{ind}}{\sim} \text{GEV}(a(\mathbf{x}_i), \exp(b(\mathbf{x}_i)), \exp(s)) \\ a(\mathbf{x}) | \sigma_a, \lambda_a &\sim \mathcal{GP}(0, k(\mathbf{x}, \mathbf{x}' | \sigma_a^2, \lambda_a)) \\ b(\mathbf{x}) | \sigma_b, \lambda_b &\sim \mathcal{GP}(0, k(\mathbf{x}, \mathbf{x}' | \sigma_b^2, \lambda_b)). \end{aligned} \quad (3)$$

The Bayesian model is completed by specifying a Lebesgue prior $\pi(\boldsymbol{\theta}) \propto 1$ on the fixed effect and hyperparameters $\boldsymbol{\theta} = (s, \log(\sigma_a^2), \log(\lambda_a), \log(\sigma_b^2), \log(\lambda_b))$.

2.1. Estimation of Fixed Effects and Hyperparameters

Let $\mathbf{y} = (\mathbf{y}_1, \dots, \mathbf{y}_n)^T$ denote the vector of observations, $\mathbf{a} = (a(\mathbf{x}_1), a(\mathbf{x}_2), \dots, a(\mathbf{x}_n))^T$ and $\mathbf{b} = (b(\mathbf{x}_1), b(\mathbf{x}_2), \dots, b(\mathbf{x}_n))^T$ denote the corresponding vectors of random effects, and let $\mathbf{u} = (\mathbf{a}, \mathbf{b})$. Then the joint distribution of data and random effects is

$$\begin{aligned} p(\mathbf{y}, \mathbf{u} | \boldsymbol{\theta}) &= \prod_{i=1}^n \prod_{k=1}^{n_i} \left\{ \frac{1}{\exp(b(\mathbf{x}_i))} (1 + \exp(s)z_{ik})^{-\frac{1+\exp(s)}{\exp(s)}} \exp \left[- (1 + \exp(s)z_{ik})^{-\frac{1}{\exp(s)}} \right] \right\} \\ &\times \frac{1}{\sqrt{(2\pi)^n |\boldsymbol{\Sigma}_a|}} \exp \left[-\frac{1}{2} \mathbf{a}^T \boldsymbol{\Sigma}_a^{-1} \mathbf{a} \right] \times \frac{1}{\sqrt{(2\pi)^n |\boldsymbol{\Sigma}_b|}} \exp \left[-\frac{1}{2} \mathbf{b}^T \boldsymbol{\Sigma}_b^{-1} \mathbf{b} \right], \end{aligned} \quad (4)$$

where $z_{ik} = (y_{ik} - a(\mathbf{x}_i)) / \exp(b(\mathbf{x}_i))$, $\boldsymbol{\Sigma}_a = [k(\mathbf{x}_i, \mathbf{x}_j | \sigma_a^2, \lambda_a)]_{1 \leq i, j \leq n}$, and $\boldsymbol{\Sigma}_b = [k(\mathbf{x}_i, \mathbf{x}_j | \sigma_b^2, \lambda_b)]_{1 \leq i, j \leq n}$.

Since the matrix inversions $\boldsymbol{\Sigma}_a^{-1}$ and $\boldsymbol{\Sigma}_b^{-1}$ in (4) are $\mathcal{O}(n^3)$, each evaluation of $p(\mathbf{y}, \mathbf{u} | \boldsymbol{\theta})$ can be very computationally intensive for large n . There are several well-known methods to increase the computational efficiency of this mixed-effects modelling approach. Sang & Gelfand (2008), Schliep et al. (2010), and Cooley & Sain (2010) adopted the conditional autoregressive (CAR) model (Besag, 1974; Besag et al., 1991) for the latent spatial process by imposing a conditional independence assumption on the spatial dependence structure among the random effects. This class of models is usually specified using a sparse precision matrix that reduces computational costs. However, the CAR model is only defined at a predetermined set of spatial locations, whereas the

more general GEV-GP model can make weather predictions at any geographical location. Within the GEV-GP modeling framework, [Lindgren et al. \(2011\)](#) developed an efficient approximation to the GP contribution in (4) using a stochastic partial differential equation (SPDE) for a different covariance kernel (see [Opitz, 2017](#), for a review of this technique). We do not explore these approximation techniques here, but note that the Laplace approximation we employ is fully compatible with either. We return to this discussion in Section 5.

For a given prior $\pi(\boldsymbol{\theta})$, a common approach in Bayesian inference is to use MCMC to draw samples from the posterior distribution

$$p(\mathbf{u}, \boldsymbol{\theta} \mid \mathbf{y}) \propto p(\mathbf{y}, \mathbf{u} \mid \boldsymbol{\theta})\pi(\boldsymbol{\theta}). \quad (5)$$

However, the mixing time of MCMC algorithms for the posterior distribution (5) can be very slow when the number of observations n is large. As an alternative to MCMC we now present a Laplace approximation to the joint posterior distribution $p(\mathbf{u}, \boldsymbol{\theta} \mid \mathbf{y})$. To describe the approximation, consider the marginal posterior distribution

$$p(\boldsymbol{\theta} \mid \mathbf{y}) \propto \mathcal{L}(\boldsymbol{\theta} \mid \mathbf{y})\pi(\boldsymbol{\theta}), \quad (6)$$

where

$$\begin{aligned} \mathcal{L}(\boldsymbol{\theta} \mid \mathbf{y}) &= \int p(\mathbf{y} \mid \mathbf{u}, \boldsymbol{\theta})p(\mathbf{u} \mid \boldsymbol{\theta}) \, d\mathbf{u} \\ &= \int \exp \{G(\mathbf{u}; \boldsymbol{\theta})\} \, d\mathbf{u}. \end{aligned} \quad (7)$$

For the GEV-GP model, this integral is intractable, which is why an MCMC over the joint posterior distribution (5) is typically used for Bayesian inference. Instead, the Laplace approximation converts the intractable integral into a tractable optimization problem as follows. Given $\boldsymbol{\theta}$, one can find

$$\mathbf{u}_{\boldsymbol{\theta}} = \underset{\mathbf{u}}{\operatorname{argmax}} G(\mathbf{u}; \boldsymbol{\theta}) \quad (8)$$

via numerical maximization. Then $G(\mathbf{u}; \boldsymbol{\theta})$ is approximated by its second-order Taylor expansion about $\mathbf{u}_{\boldsymbol{\theta}}$, i.e.,

$$G(\mathbf{u}; \boldsymbol{\theta}) \approx G(\mathbf{u}_{\boldsymbol{\theta}}; \boldsymbol{\theta}) + \frac{1}{2}(\mathbf{u} - \mathbf{u}_{\boldsymbol{\theta}})^T \mathbf{H}_{\boldsymbol{\theta}}(\mathbf{u} - \mathbf{u}_{\boldsymbol{\theta}}), \quad (9)$$

where $[\mathbf{H}_{\boldsymbol{\theta}}]_{1 \leq i, j \leq n} = \frac{\partial^2}{\partial \mathbf{u} \partial \mathbf{u}^T} G(\mathbf{u}_{\boldsymbol{\theta}}; \boldsymbol{\theta})$, and the first-order term vanishes since the gradient of $G(\mathbf{u}; \boldsymbol{\theta})$ equals zero at the mode $\mathbf{u}_{\boldsymbol{\theta}}$. Let $\phi(\mathbf{z} \mid \boldsymbol{\mu}, \boldsymbol{\Sigma})$ denote the PDF of $\mathbf{z} \sim \mathcal{N}(\boldsymbol{\mu}, \boldsymbol{\Sigma})$. Substituting the Taylor expansion (9) into (7) gives

$$\begin{aligned} \tilde{\mathcal{L}}(\boldsymbol{\theta} \mid \mathbf{y}) &= \int \exp \left\{ G(\mathbf{u}_{\boldsymbol{\theta}}; \boldsymbol{\theta}) + \frac{1}{2}(\mathbf{u} - \mathbf{u}_{\boldsymbol{\theta}})^T \mathbf{H}_{\boldsymbol{\theta}}(\mathbf{u} - \mathbf{u}_{\boldsymbol{\theta}}) \right\} \, d\mathbf{u} \\ &\propto \exp \left\{ G(\mathbf{u}_{\boldsymbol{\theta}}; \boldsymbol{\theta}) - \frac{1}{2} \log |\mathbf{H}_{\boldsymbol{\theta}}| \right\} \cdot \int \phi(\mathbf{u} \mid \mathbf{u}_{\boldsymbol{\theta}}, \mathbf{H}_{\boldsymbol{\theta}}^{-1}) \, d\mathbf{u} \\ &= \exp \left\{ G(\mathbf{u}_{\boldsymbol{\theta}}; \boldsymbol{\theta}) - \frac{1}{2} \log |\mathbf{H}_{\boldsymbol{\theta}}| \right\}. \end{aligned} \quad (10)$$

In a Bayesian context, the Laplace approximation may be used to construct a Normal approximation to the marginal posterior distribution,

$$\boldsymbol{\theta} \mid \mathbf{y} \approx \mathcal{N}(\widehat{\boldsymbol{\theta}}, \widehat{\mathbf{V}}_{\boldsymbol{\theta}}), \quad (11)$$

where $\widehat{\boldsymbol{\theta}} = \underset{\boldsymbol{\theta}}{\operatorname{argmax}} \tilde{p}(\boldsymbol{\theta} \mid \mathbf{y})$ is the mode of the Laplace posterior approximation

$$\tilde{p}(\boldsymbol{\theta} \mid \mathbf{y}) \propto \tilde{\mathcal{L}}(\boldsymbol{\theta} \mid \mathbf{y})\pi(\boldsymbol{\theta}), \quad (12)$$

and $\widehat{\mathbf{V}}_{\boldsymbol{\theta}} = -\left[\frac{\partial^2}{\partial \boldsymbol{\theta}^2} \log \tilde{p}(\widehat{\boldsymbol{\theta}} \mid \mathbf{y})\right]^{-1}$ is the quadrature of the log-posterior about the mode calculated at $\boldsymbol{\theta} = \widehat{\boldsymbol{\theta}}$.

2.2. Estimation of Random Effects

The next step is to estimate $p(\mathbf{u} \mid \mathbf{y})$, the marginal posterior distribution of the random effects \mathbf{u} . Since $p(\mathbf{u} \mid \mathbf{y}) = \int p(\mathbf{u} \mid \boldsymbol{\theta}, \mathbf{y})p(\boldsymbol{\theta} \mid \mathbf{y}) d\boldsymbol{\theta}$, it depends on the posterior distribution of $\boldsymbol{\theta}$. One way to estimate $p(\mathbf{u} \mid \mathbf{y})$ is via a two-step sampling scheme. That is, first simulate $\boldsymbol{\theta}_1^s, \boldsymbol{\theta}_2^s, \dots, \boldsymbol{\theta}_m^s$ from $\tilde{p}(\boldsymbol{\theta} \mid \mathbf{y})$ via the Normal distribution (11). For each simulated $\boldsymbol{\theta}_i^s$, approximate the conditional posterior random effects distribution $p(\mathbf{u} \mid \boldsymbol{\theta}_i^s, \mathbf{y})$ by a multivariate Normal with mean $\mathbf{u}_{\boldsymbol{\theta}_i^s} = \underset{\mathbf{u}}{\operatorname{argmax}} G(\mathbf{u}; \boldsymbol{\theta}_i^s)$ and variance $\widehat{\mathbf{V}}_{\mathbf{u}}(\boldsymbol{\theta}_i^s) = -\left[\frac{\partial^2}{\partial \mathbf{u} \partial \mathbf{u}^T} G(\mathbf{u}_{\boldsymbol{\theta}_i^s}; \boldsymbol{\theta}_i^s)\right]^{-1}$. Then draw $\mathbf{u}_i^s \sim \mathcal{N}(\mathbf{u}_{\boldsymbol{\theta}_i^s}, \widehat{\mathbf{V}}_{\mathbf{u}}(\boldsymbol{\theta}_i^s))$. However, this procedure is computationally intensive as numerical optimization is involved at each sampling step to find the conditional mean and covariance of the Normal distribution. We propose a simplified and much faster method to approximate $p(\mathbf{u} \mid \mathbf{y})$ as follows.

Conditional on $\boldsymbol{\theta}$ and \mathbf{y} , the posterior distribution of \mathbf{u} can be approximated by a Normal distribution

$$\mathbf{u} \mid \boldsymbol{\theta}, \mathbf{y} \approx \mathcal{N}(\mathbf{u}_{\boldsymbol{\theta}}, \widehat{\mathbf{V}}_{\mathbf{u}}(\boldsymbol{\theta})), \quad (13)$$

where the mean $\mathbf{u}_{\boldsymbol{\theta}}$ and the covariance matrix $\widehat{\mathbf{V}}_{\mathbf{u}}(\boldsymbol{\theta})$ are functions of $\boldsymbol{\theta}$. Applying a first-order Taylor expansion of $\mathbf{u}_{\boldsymbol{\theta}}$ and a zeroth-order Taylor expansion of $\widehat{\mathbf{V}}_{\mathbf{u}}(\boldsymbol{\theta})$ about $\boldsymbol{\theta} = \widehat{\boldsymbol{\theta}}$, these two functions are approximated by

$$\mathbf{u}_{\boldsymbol{\theta}} \approx \mathbf{u}_{\widehat{\boldsymbol{\theta}}} + \mathbf{J}_{\mathbf{u}}(\boldsymbol{\theta} - \widehat{\boldsymbol{\theta}}), \quad (14)$$

$$\widehat{\mathbf{V}}_{\mathbf{u}}(\boldsymbol{\theta}) \approx \widehat{\mathbf{V}}_{\mathbf{u}}(\widehat{\boldsymbol{\theta}}), \quad (15)$$

where $\mathbf{J}_{\mathbf{u}} = \left[\frac{\partial}{\partial \boldsymbol{\theta}} u_{\boldsymbol{\theta},1} \cdots \frac{\partial}{\partial \boldsymbol{\theta}} u_{\boldsymbol{\theta},n}\right]^T$ with $u_{\boldsymbol{\theta},i}$ being the i^{th} element of the vector $\mathbf{u}_{\boldsymbol{\theta}}$. Note that if \mathbf{u} and $\boldsymbol{\theta}$ are assumed to follow a joint Normal distribution, then the conditional mean of \mathbf{u} given $\boldsymbol{\theta}$ is linear in $\boldsymbol{\theta}$, which agrees with Equation (14), and the conditional covariance matrix is constant, which matches Equation (15). Therefore, combining equations (11), (14) and (15) we obtain the Normal approximation to the joint posterior of \mathbf{u} and $\boldsymbol{\theta}$:

$$\mathbf{u}, \boldsymbol{\theta} \mid \mathbf{y} \approx \mathcal{N}\left(\begin{pmatrix} \mathbf{u}_{\widehat{\boldsymbol{\theta}}} \\ \widehat{\boldsymbol{\theta}} \end{pmatrix}, \begin{pmatrix} \widehat{\mathbf{V}}_{\mathbf{u}}(\widehat{\boldsymbol{\theta}}) + \mathbf{J}_{\mathbf{u}} \widehat{\mathbf{V}}_{\boldsymbol{\theta}} \mathbf{J}_{\mathbf{u}}^T & \mathbf{J}_{\mathbf{u}} \widehat{\mathbf{V}}_{\boldsymbol{\theta}} \\ \widehat{\mathbf{V}}_{\boldsymbol{\theta}} \mathbf{J}_{\mathbf{u}}^T & \widehat{\mathbf{V}}_{\boldsymbol{\theta}} \end{pmatrix}\right). \quad (16)$$

Therefore, the computationally intensive two-step sampling scheme above is replaced by the much faster method of sampling directly from the joint posterior in Equation (16).

2.3. Implementation

The calculation of the posterior mode $\hat{\boldsymbol{\theta}} = \underset{\boldsymbol{\theta}}{\operatorname{argmax}} \tilde{p}(\boldsymbol{\theta} \mid \mathbf{y})$ is a nested optimization problem, since an inner optimization $\mathbf{u}_{\boldsymbol{\theta}} = \underset{\mathbf{u}}{\operatorname{argmax}} G(\mathbf{u}; \boldsymbol{\theta})$ is performed at each step of the outer optimization of $\tilde{p}(\boldsymbol{\theta} \mid \mathbf{y})$. Moreover, various first- and second-order derivatives are required at different stages of the optimizations and in the calculation of the joint posterior distribution (16). We provide an efficient C++ implementation of these computations using automatic differentiation techniques tailored to the Laplace approximation, as provided by the R/C++ package TMB (Kristensen et al., 2016). Our implementation is provided in the R/C++ package SpatialGEV (Chen et al., 2021).

3. Simulation Study

The interest of extreme weather modelling often lies in estimating the return level, which is the $p \times 100\%$ upper quantile of the extreme value distribution at a given spatial location \mathbf{x} (Coles, 2001). We denote this quantity by $z_p(a(\mathbf{x}), b_o(\mathbf{x}), s_o(\mathbf{x}))$, or simply as $z_p(\mathbf{x})$ when there is no confusion, which can be calculated, using (1) for the GEV distribution, by

$$\begin{aligned} z_p(a(\mathbf{x}), b_o(\mathbf{x}), s_o(\mathbf{x})) &= F^{-1}(1 - p \mid a(\mathbf{x}), b_o(\mathbf{x}), s_o) \\ &= \begin{cases} a(\mathbf{x}) - \frac{b_o(\mathbf{x})}{s_o} \{1 - [-\log(1 - p)]^{-s_o}\} & s_o \neq 0, \\ a(\mathbf{x}) - b_o(\mathbf{x}) \log[-\log(1 - p)] & s_o = 0. \end{cases} \end{aligned} \quad (17)$$

With extreme rainfalls as an example, $z_p(\mathbf{x})$ is interpreted as the value above which precipitation levels at a given location \mathbf{x} occur with probability p . Therefore, it is an indicator of how extreme an event might be at a given location when p is chosen to be a small number. At any given location \mathbf{x} , the posterior distribution $p(z_p(\mathbf{x}) \mid \mathbf{y})$ is simulated by computing (17) for $n_{\text{sim}} = 10,000$ simulations of $(a(\mathbf{x}), b_o(\mathbf{x}), s_o(\mathbf{x}))$, which is obtained by transforming draws of $(\mathbf{u}, \boldsymbol{\theta})$ from (16). We then use the posterior mean $E(z_p(\mathbf{x}) \mid \mathbf{y})$ as the Bayesian point estimator of $z_p(\mathbf{x})$, with its associated 95% credible interval given by the lower 2.5% and upper 97.5% quantiles of $p(z_p(\mathbf{x}) \mid \mathbf{y})$. This knowledge about the posterior distribution of return levels can be used to forecast extreme events. In order to investigate the speed and accuracy of our Laplace approximation, the following simulation study is proposed.

The study consists of spatial locations on a 20×20 regular lattice on $[0, 10] \times [0, 10] \subset \mathbb{R}^2$, such that there are $n = 400$ observations in total. The corresponding $a(\mathbf{x}_i)$ and $b(\mathbf{x}_i)$ are set deterministically via the functions

$$a(\mathbf{x}) = -0.2 \log(2\pi) - 0.1 \cdot \log \{ \det(\boldsymbol{\Sigma}_0) \} - 0.1 \cdot (\mathbf{x} - \boldsymbol{\mu}_0)^T \boldsymbol{\Sigma}_0^{-1} (\mathbf{x} - \boldsymbol{\mu}_0) + 6, \quad (18)$$

$$\begin{aligned} b(\mathbf{x}) &= 0.07 \cdot \log \left\{ 0.64 \cdot \det(\boldsymbol{\Sigma}_1)^{-\frac{1}{2}} \exp \left(-\frac{1}{2} (\mathbf{x} - \boldsymbol{\mu}_1)^T \boldsymbol{\Sigma}_1^{-1} (\mathbf{x} - \boldsymbol{\mu}_1) \right) \right. \\ &\quad \left. + 0.09 \cdot \det(\boldsymbol{\Sigma}_2)^{-\frac{1}{2}} \exp \left(-\frac{1}{2} (\mathbf{x} - \boldsymbol{\mu}_2)^T \boldsymbol{\Sigma}_2^{-1} (\mathbf{x} - \boldsymbol{\Sigma}_2) \right) \right\} + 0.14, \end{aligned} \quad (19)$$

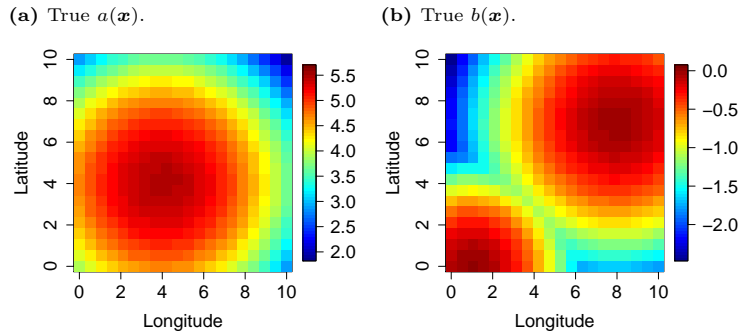


Figure 1: The true $a(\mathbf{x}_i)$ and $b(\mathbf{x}_i)$ plotted on regular lattices.

where

$$\boldsymbol{\mu}_0 = \begin{pmatrix} 4 \\ 4 \end{pmatrix}, \boldsymbol{\Sigma}_0 = \begin{pmatrix} 2 & 0 \\ 0 & 2 \end{pmatrix}, \boldsymbol{\mu}_1 = \begin{pmatrix} 1 \\ 0 \end{pmatrix}, \boldsymbol{\Sigma}_1 = \begin{pmatrix} 0.5 & 0 \\ 0 & 0.5 \end{pmatrix}, \boldsymbol{\mu}_2 = \begin{pmatrix} 8 \\ 7 \end{pmatrix}, \boldsymbol{\Sigma}_2 = \begin{pmatrix} 1 & 0 \\ 0 & 1 \end{pmatrix}.$$

Heat maps for $a(\mathbf{x})$ and $b(\mathbf{x})$ on the spatial domain are displayed in Figure 1a and 1b. Finally, we fix the shape parameter at $s = -2$ on the log scale, which correspond to $s_o = 0.135$ on the original scale. This value is chosen based on the study of Cooley & Sain (2010), in which the shape parameter for various precipitation models ranged between 0 and 0.2. Exploratory analyses also showed that under the same $a(\mathbf{x})$ and $b(\mathbf{x})$ settings, the accuracy of the estimation of $b(\mathbf{x})$ noticeably decreases when $s > -1$. This is due to the fact that the quality of the estimation of the scale parameter depends on the tail of the GEV distribution, which itself is a function of s . To demonstrate that our method is viable even on the extreme case where there is only one observation per location, our simulation study includes only one observation per location, i.e. $n_i = 1$ for all i . The results for replicated observations are omitted here.

We compare the performance of our Laplace method to both INLA and MCMC on the joint posterior $p(\mathbf{u}, \boldsymbol{\theta} \mid \mathbf{y})$. For inference with INLA, we adopt the fast SPDE approximation to the covariance kernel as implemented in the R-INLA package (Lindgren & Rue, 2015). Since the INLA method is not applicable to modelling both the GEV location and scale parameters as spatially varying, we use it to model only $a(\mathbf{x})$ as a Gaussian process and model the scale parameter b as a fixed effect. The MCMC algorithm we use is the No-U-Turn sampling (NUTS) variant of HMC (Hoffman & Gelman, 2014) as implemented in the R/C++ library RStan (Stan Development Team, 2020). Four Markov chains were run in parallel for 500 iterations (post burn-in) per chain. The number of iterations was chosen post-hoc to ensure that the effective sample sizes are approximately 400, which is in line with the recommendation in Vehtari et al. (2021). We checked that all chains have mixed well based on the $\widehat{R} < 1.05$ convergence metric advocated in Vehtari et al. (2021). The MCMC method is taken as the benchmark for accuracy comparisons, since its results are the closest we can get to the exact posteriors.

Figure 2 shows the scatterplots of the posterior mean estimates of $a(\mathbf{x})$ and $b(\mathbf{x})$ versus their true values using the different methods, as well as the true and estimated values of s . The Laplace

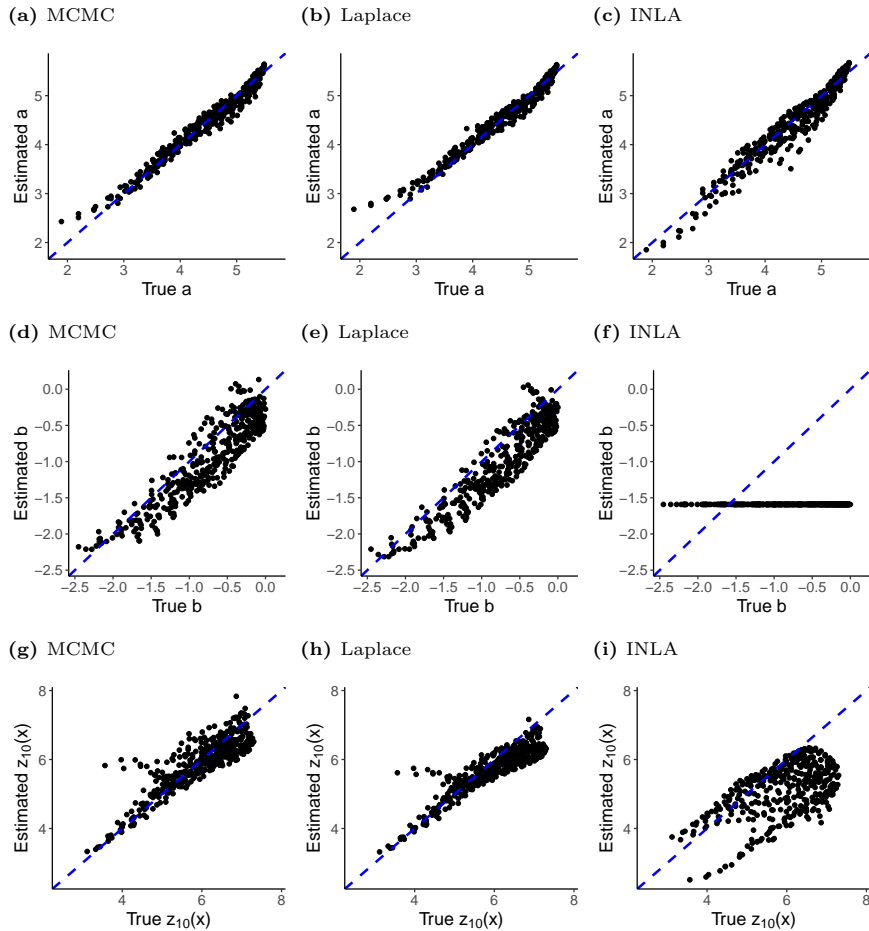


Figure 2: True GEV location parameters $a(\mathbf{x})$, scale parameters $b(\mathbf{x})$ and return levels $z_{10}(\mathbf{x})$ plotted against their estimates obtained using MCMC, Laplace, and INLA. The true log shape parameter $s = -2.00$. The corresponding Laplace method estimate $\hat{s}_{La} = -1.90$ with a 95% credible interval $[-2.56, -1.26]$, whereas the MCMC estimate $\hat{s}_{MCMC} = -1.48$ with a 95% credible interval $[-2.25, -0.98]$, and the INLA estimate $\hat{s}_{INLA} = -1.25$ with a 95% credible interval $[-1.73, -0.96]$.

method slightly underestimates the location parameter and correspondingly overestimates the scale parameter. However, the same pattern occurs with the MCMC method, indicating that the Laplace approximation is accurately representing the true posterior means. With more observations at each location, one can expect higher accuracy in the estimation of all parameters, in particular, the scale parameter.

Interestingly, for $a(\mathbf{x}) < 3$, the estimated $a(\mathbf{x})$ from INLA align better with the true values than those from the exact posteriors given by MCMC. However, the estimates deviate more from the true values for $a(\mathbf{x}) \geq 3$, and a single estimate of b is produced for all locations, as indicated by the horizontal line in Figure 2f. In contrast, our Laplace method is extremely close to the exact posteriors for both $a(\mathbf{x})$ and $b(\mathbf{x})$. As for s , the Laplace estimate $\hat{s}_{La} = -1.9$ is close to the true value $s = -2$, with a 95% credible interval of $[-2.56, -1.26]$. Based on our simulation experiments and also according to the literature (Coles & Casson, 1998; Cooley & Sain, 2010; Ghosh & Mallick,

	a and b random, s fixed		a random, s and b fixed	
	MCMC	Laplace	INLA	Laplace
$\text{MAE}(\hat{a}(\mathbf{x})) = \frac{\sum_{i=1}^n a(\mathbf{x}_i) - \hat{a}(\mathbf{x}_i) }{n}$	0.101	0.0961	0.148	0.153
$\text{MAE}(\hat{b}(\mathbf{x})) = \frac{\sum_{i=1}^n b(\mathbf{x}_i) - \hat{b}(\mathbf{x}_i) }{n}$	0.269	0.292	0.491	0.911
$\text{AE}(\hat{s}) = s - \hat{s} $	0.520	0.0974	0.789	0.883
Time	8000(\pm 1000)s	87(\pm1)s	13(\pm 0.5)s	36(\pm 0.5)s

Table 1: Comparison of MCMC, the Laplace method, and INLA.

2011), the estimation of s is more accurate when s_o lies in a practical range, i.e. $s_o < 0.3$ on the original scale. The estimated s from MCMC is $\hat{s}_{\text{MCMC}} = -1.48$ and the corresponding 95% credible interval is $[-2.25, -0.98]$, indicating that the Laplace estimate is slightly shifted from the true posterior. The INLA estimate $\hat{s}_{\text{INLA}} = -1.25$ is somewhat less accurate, and the 95% credible interval $[-1.73, -0.96]$ does not cover the true value. Thus, we surmise that inaccurate estimation of $a(\mathbf{x})$ and s is due to INLA treating b as a fixed effect.

To highlight the importance of modelling both location and scale GEV parameters as spatially-varying, we turn to the estimation of the meteorological quantity of interest: the return level (17). At each location, the Bayesian point estimate of the 10% return level $z_{10}(\mathbf{x})$ is computed. Figure 2g, 2h, and 2i show the estimates obtained from MCMC, the Laplace method, and INLA as functions of the true return levels. It is found that the INLA approach significantly underestimates $z_{10}(\mathbf{x})$ compared to MCMC and Laplace. From a practical standpoint, severe underestimation of return levels can result in failure to anticipate weather hazards. Therefore, the ability to model both $a(\mathbf{x})$ and $b(\mathbf{x})$ as spatially-varying parameters can be of crucial importance for weather forecasting.

Table 1 reports the numerical summary of accuracy results as well as timing. The evaluation metrics are the absolute error for s and mean absolute errors for $a(\mathbf{x})$ and $b(\mathbf{x})$ at the $n = 400$ spatial locations, as well as computation time. Compared to MCMC, our method is around two orders of magnitude faster while obtaining similar accuracy for estimating $a(\mathbf{x})$ and $b(\mathbf{x})$. Since INLA restricts the model to only one spatially varying predictor (in this case $a(\mathbf{x})$), we cannot directly compare the speed of our method to that of INLA due to different model complexities. Therefore, we use the Laplace approximation to fit a simplified version of our GEV-GP model so that only the location parameter $a(\mathbf{x})$ is modelled by a Gaussian process, keeping both the scale and shape parameters as fixed effects. Within this restricted setup, our method is slightly less accurate than INLA. Notably, INLA is considerably faster than our Laplace method even though it is a more sophisticated approximation method. Ostensibly, this is due to the SPDE approximation which INLA employs to accelerate the calculation of Gaussian process likelihoods. Thus, the Laplace stands to be significantly accelerated if we were to use this approximation as well.

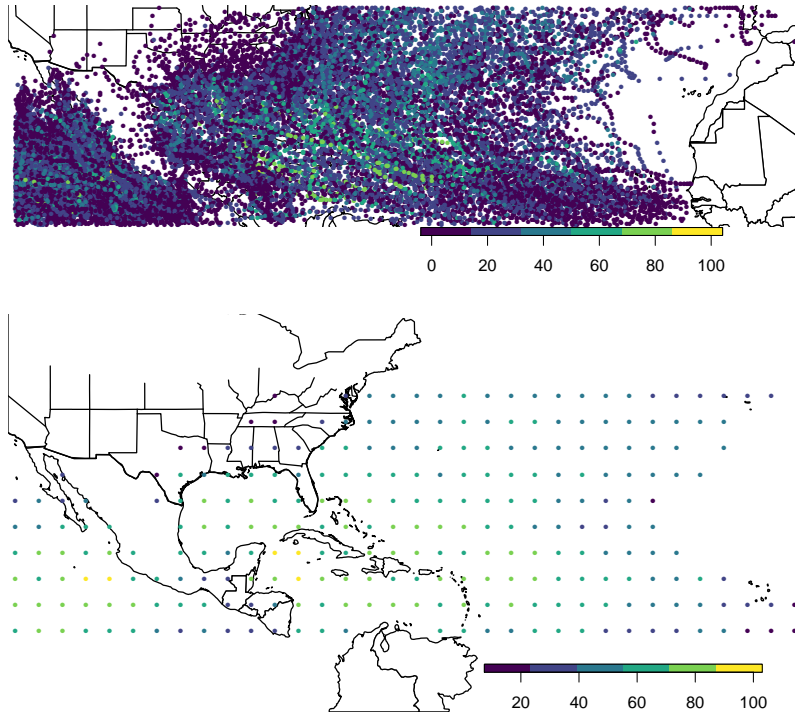


Figure 3: Upper panel: Raw data from 1980 to 2015 with each point color-coded by the wind speed value. Lower panel: Gridded data with only the maximum wind speed attained in each cell.

4. Case Study

The International Best Track Archive for Climate Stewardship (IBTrACS) dataset (Knapp et al., 2010) is the global set of tropical cyclone data over more than a hundred years. The intensity of a tropical cyclone can be quantified by its 1-minute maximum sustained wind speed, which is the highest average of the measured winds at a 10-meter height for one minute. For example, if the 1-minute maximum sustained wind speed reaches 33m/s, the cyclone is classified as a hurricane. In the remainder of this section, wind speed refers to the 1-minute maximum sustained wind speed in m/s. For this analysis we consider a subset of the IBTrACS dataset restricted to an area of North Atlantic Ocean from 1980 to 2015. It is noteworthy that this dataset is characterized by large spatiotemporal coverage and an unconventional data format. Unlike datasets consisting of repeated observations at a small number of weather stations, the IBTrACS dataset is a collection of different tropical cyclone trajectories and contains the wind data recorded every 6 hours along each trajectory. For every cyclone, the dataset tracks its coordinates every 6 hours and records the wind speed at that coordinate, thereby providing a map of winds with a high spatiotemporal resolution.

The upper panel of Figure 3 shows the raw data pooled over 35 years with each point color-coded by the wind speed value. In the bottom panel of Figure 3, the data are gridded into $3^\circ \times 3^\circ$

Model	M_1	M_2	M_3	M_4	M_5
Location parameter a	RE	RE	RE	RE	RE
Scale parameter b	RE	RE	RE	FE	FE
Shape parameter s_o	Positive FE	Zero	Zero	Zero	Zero
Data transformation	None	None	Log	None	None
Fitting method	Laplace	Laplace	Laplace	Laplace	INLA

Table 2: Five models of different complexities on the IBTrACS dataset. RE stands for (spatial) random effect, and FE stands for fixed effect.

cells. We only include cells in which there are at least 20 wind records across the observed years, and in line with extreme value theory, use the maximum record in each cell as the response value. In the following analysis, we refer to each cell as a location whose coordinates are at the center of the cell. Thus, our analysis involves $n = 264$ spatial locations (grid cells) each with one extreme value observation.

4.1. Model Selection

We compare five GEV-GP models of different complexities for this wind speed dataset. The model information is summarized in Table 2. All five models treat the location parameter a as a spatially varying random effect $a(\mathbf{x})$ as the spatial variation in $a(\mathbf{x})$ contributes greatly to the wind speed variation across different locations. The scale parameter b is modelled as a random effect $b(\mathbf{x})$ in models M_1 , M_2 , and M_3 but considered as a fixed effect in models M_4 and M_5 . The shape parameter s is considered a fixed effect to be estimated in model M_1 . Models M_2 to M_5 simply let $s_o = 0$, which corresponds to the Gumbel distribution – a so-called “Type I” GEV distribution with lighter tails – which is a common choice in the literature for extreme wind speeds (Palutikof et al., 1999). A logarithmic transformation is applied on the data in model M_3 to determine if the model fits better on the log scale.

The fit of each model to the iBTrACS dataset is first evaluated by the following coverage check. For a given value of $p_{\text{exp}} \in (0, 1)$, let $L(\mathbf{x}_*)$ and $U(\mathbf{x}_*)$ denote the $(1 - p_{\text{exp}})/2$ and $1 - (1 - p_{\text{exp}})/2$ quantiles of the posterior predictive distribution of maximum wind speed y_* at spatial location \mathbf{x}_* ,

$$p(y_* | \mathbf{y}) = \int p(y_* | a(\mathbf{x}_*), b(\mathbf{x}_*), s) p(a(\mathbf{x}_*), b(\mathbf{x}_*), s | \mathbf{y}) da(\mathbf{x}_*) db(\mathbf{x}_*) ds. \quad (20)$$

The calculations of the posterior predictive distribution and $(L(\mathbf{x}_*), U(\mathbf{x}_*))$ is detailed in Appendix A.

Now suppose that p_{obs} is the fraction of the observed y_i , $i = 1, \dots, 264$ which are between $L(\mathbf{x}_i)$ and $U(\mathbf{x}_i)$, for $i = 1, \dots, n$. If the model is correctly specified, then one should have $p_{\text{obs}} \approx p_{\text{exp}}$. Figure 4 plots p_{obs} vs p_{exp} for each of the five models in Table 2, where lack of fit is indicated by departures from the 45° line.

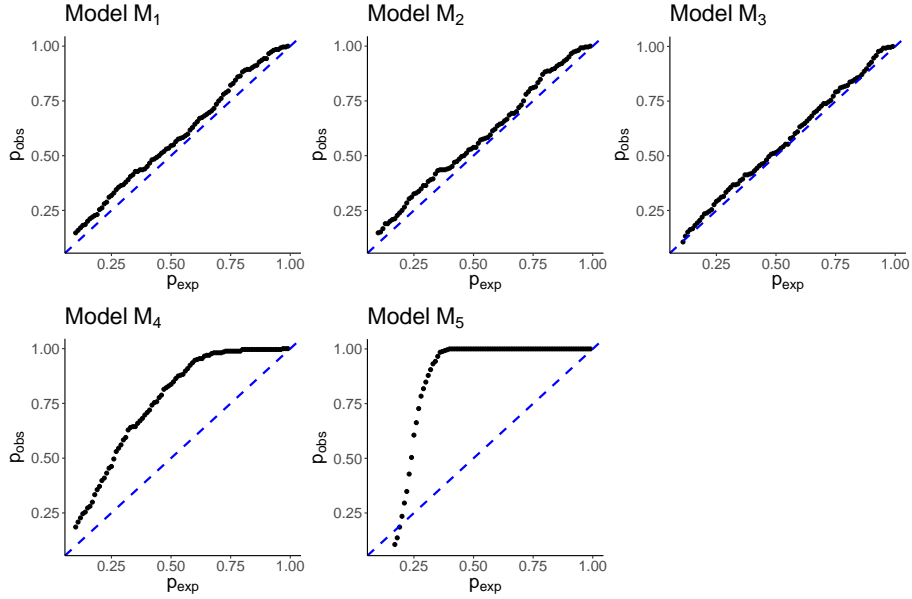


Figure 4: Coverage plots for the candidate models. The x-axis is the expected coverage rate p_{exp} : $\{0.1, 0.11, 0.12, \dots, 0.98, 0.99\}$, whereas the y-axis is the proportion of locations at which the observed wind speed lies in the corresponding $100p_{\text{exp}}\%$ posterior predictive interval: p_{obs} .

Models M_4 and M_5 have substantially worse coverage plots than the other three models, once again underscoring the importance of having the ability to model both location and scale parameters of the GEV distribution as spatially varying. The coverage plots for M_1 and M_2 look almost identical even though M_1 estimates an additional parameter s . It is found that s is estimated to be -10.1 on the log scale with a 95% credible interval of $(-19.63, -0.56)$ under M_1 . This implies that the data estimates a very small value of s_o , which in turn suggests choosing M_2 and M_3 using the Gumbel distribution over M_1 for simplicity and improved estimation for other model parameters. To compare M_2 and M_3 , we first note that the true and expected coverage rates align slightly closer for M_3 whose only difference from M_2 is the log data transformation. It should also be pointed out that the support of the Gumbel distribution is \mathbb{R} , which does not provide a lower bound of zero for wind speed. This would not be an issue when fitting the model to log-transformed data, as is the case for M_3 . However, even without a log transformation, the probability of obtaining a negative value from the Gumbel distribution fit to this dataset at any spatial location is at most 6%. As a result, the unbounded support issue only has a minor impact on the posterior prediction of wind speeds when no transformation is applied.

The comparison between M_2 and M_3 can be made from a more practical point of view by investigating their out-of-sample performance. We perform the posterior predictive coverage check by first fitting the model on a training set, and then making posterior predictions on a test set. We hold off 50 randomly selected locations as the test set, which is around 20% of the whole dataset. For each test location \mathbf{x}_* , we obtain the mean and a 95% posterior predictive interval $(L(\mathbf{x}_*), U(\mathbf{x}_*))$. Figure 5 displays for each model a scatterplot of posterior means versus observed

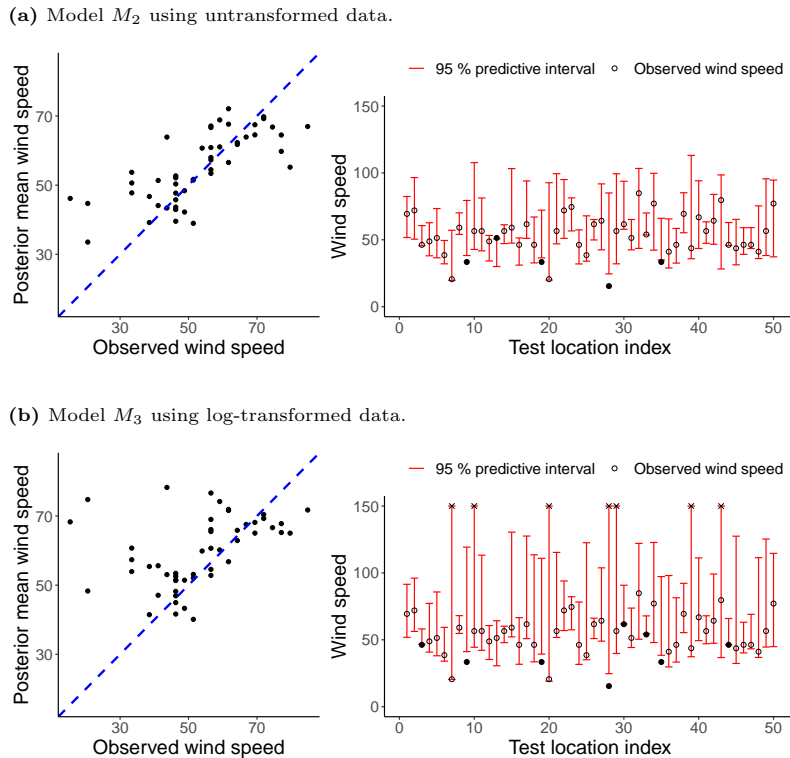


Figure 5: Posterior predictive check of models M_2 and M_3 . The scatterplots show the posterior mean prediction versus the observed wind speed at each test location. The red vertical bars on the right are the 95% posterior predictive intervals at test locations. The y-axis is truncated at 150m/s such that the truncated upper bounds are annotated by \times symbols. Each dot corresponds to the observed wind speed at a test location, with hollow ones indicating that they are inside the 95% PI, and solid ones indicating that they are outside of the 95% PI.

wind speeds, and a plot of the predictive intervals as vertical bars superimposed on the observed wind speeds. The upper bound of the predictive intervals are truncated at 150m/s. Compared to the scatterplot for M_2 , that of M_3 shows a larger number of locations at which the posterior mean is much higher than the true observation. We found that the locations for which this difference is greatest tend to lie on the boundary of the study region. That is, predictive inference is less reliable at locations with few neighbours. The right-hand-side panels of Figure 5a and 5b visualize the coverage of the 95% posterior predictive intervals at the corresponding location. It is observed that 4 out of 50 observations are not covered when using M_2 , whereas 8 are not covered when using M_3 . Moreover, prediction intervals constructed from M_3 are extremely wide at locations with high uncertainty such as location 20 and 28. This is a result of exponentiating the lower and upper bounds of the prediction intervals on the log scale. This posterior predictive check was repeated using different random seeds to generate different sets of test data, where a similar conclusion was obtained in each experiment. Therefore, we may conclude that M_2 produces more reasonable point and interval predictions of wind speeds at new locations. Further analyses will be performed based on model M_2 in the remainder of this section.

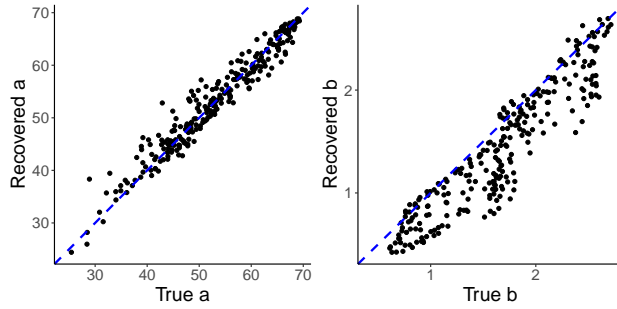


Figure 6: Recovered parameter values plotted against the true parameter values. The true parameter values are the posterior means obtained by fitting model M_2 to the IBTrACS data, whereas the recovered parameter values are obtained by refitting the model to pseudo-data simulated using the true parameters.

4.2. Refitting Assessment of the Laplace Approximation

Given that this is a real data study and the true parameter values are unknown, we would like to check the accuracy of the Laplace approximation on synthetic data which mimic the real data. It was shown in Section 3 that the model with random effects $a(\mathbf{x})$ and $b(\mathbf{x})$ and a fixed effect s can recover the true parameters reasonably well. Now, instead of generating the GEV parameters from predefined deterministic functions, we use the posterior means of the GEV parameters $a(\mathbf{x})$, $b(\mathbf{x})$, and s obtained by fitting model M_2 to the IBTrACS dataset. These values are then used as the true parameter values to simulate pseudo-data from the GEV distribution. The model is refitted on the pseudo-data to produce a new set of point estimates of the GEV parameters, which are then compared graphically to the true parameter values in Figure 6. It is found that the recovered parameters align closely with the true parameters for both $a(\mathbf{x})$ and $b(\mathbf{x})$, thus suggesting that the Laplace approximation is reasonably accurate for the dataset at hand. This result also provides further support to the conclusion in Section 3 that the GEV-GP model can recover the true parameters by employing a different set of GEV parameters that indeed generate real data.

4.3. Posterior Inference

The posterior means and standard deviations of model parameters at each location are plotted on the top and middle panels of Figure 7. Spatial patterns are observed for the values of $\hat{a}(\mathbf{x}) = E[a(\mathbf{x}) | \mathbf{y}]$ and $\hat{b}(\mathbf{x}) = E[b(\mathbf{x}) | \mathbf{y}]$ across the region, with higher values of $\hat{a}(\mathbf{x})$ and lower values of $\hat{b}(\mathbf{x})$ at the center of the study region. We note that the uncertainty is higher for both $a(\mathbf{x})$ and $b(\mathbf{x})$ at the coordinates near $(-85, 35)$, where data is most sparse. Plotted in the bottom panel of Figure 7 are the posterior 10% return level estimates $\hat{z}_{10}(\mathbf{x}) = E[z_{10}(\mathbf{x}) | \mathbf{y}]$ and their corresponding uncertainty levels. These two maps are helpful in practice since they provide a guide to interpret the risk of extreme winds. For example, given $\hat{z}_{10}(\mathbf{x}) \approx 45$ at the coordinate $\mathbf{x} = (-25, 40)$, we can say that there is 10% chance that the wind speed will exceed 45m/s at this location, and that we are relatively confident in this statement because of the low uncertainty level indicated in the uncertainty plot Figure 7f at the corresponding location. In contrast, there is a 10% chance

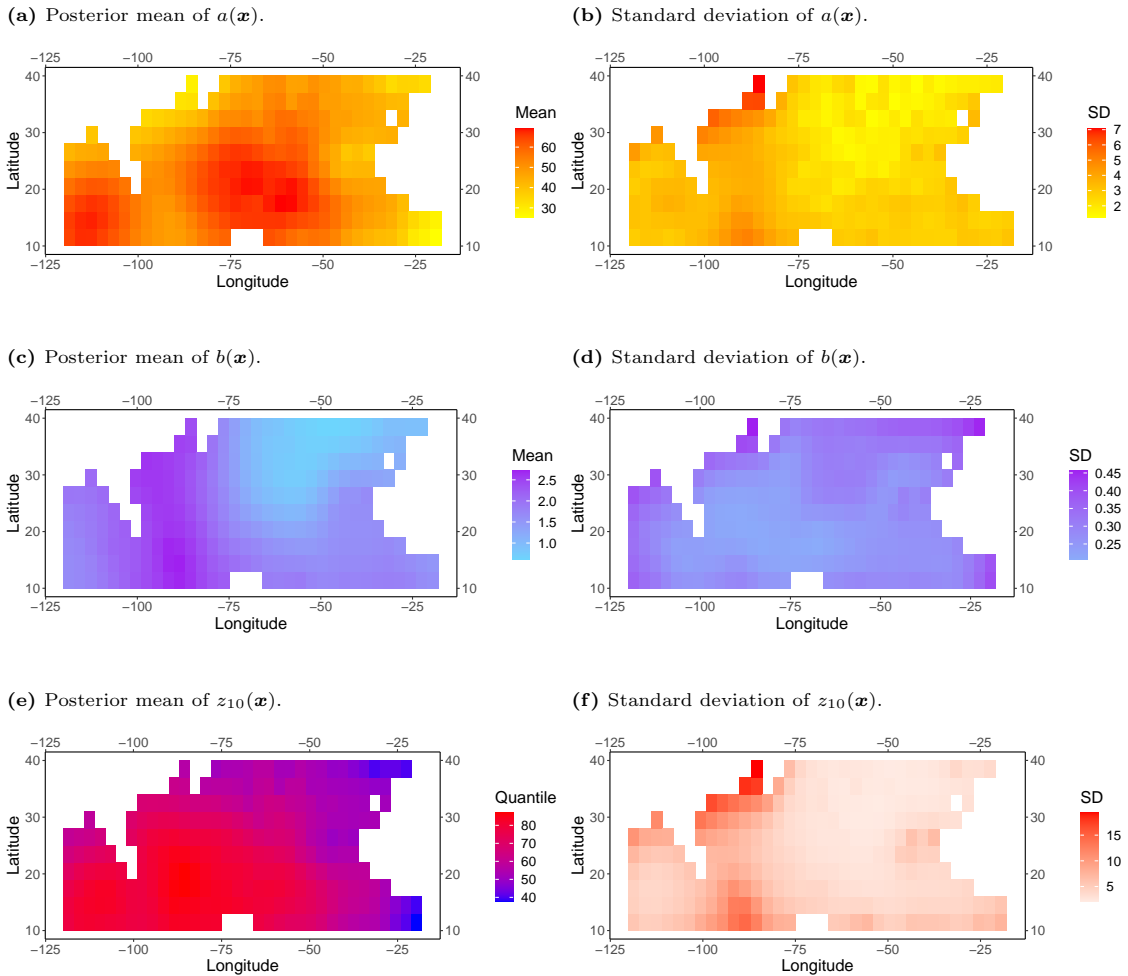


Figure 7: Posterior means and standard deviations of $a(\mathbf{x})$, $b(\mathbf{x})$, and $z_{10}(\mathbf{x})$ plotted at the corresponding coordinates.

of observing a wind speed as high as 80m/s near $(-90, 10)$, though the associated uncertainty is higher as the standard deviation is roughly 12. Given the large uncertainty in estimating the 10% return level in this geographical area, more information must be gathered around coordinate $(-85, 35)$ to make meaningful predictions there about extreme weather events.

5. Discussion

In this paper, we developed a fast method of Bayesian inference for fitting GEV-GP models, which have a wide range of applications in studying weather extremes. The proposed method applies the Laplace approximation for calculating the marginal likelihood and a Normal approximation based on a Taylor expansion to obtain the posterior distributions of the random effects. We provide an efficient C++ implementation of our method which leverages automatic differentiation in the R package `SpatialGEV`. Through simulation studies, we have shown that the proposed approximation is highly accurate and also much faster than a state-of-the-art MCMC algorithm,

which is commonly used to fit hierarchical models such as the GEV-GP. The INLA method is a popular alternative to MCMC which has been used successfully in many analyses of weather extremes (e.g., [Opitz et al., 2018](#); [Castro-Camilo et al., 2019, 2020](#)). However, INLA cannot be used for GEV-GP models with more than one spatial random effect. Such flexibility can be crucial for accurate prediction of weather extreme values, as demonstrated both via simulation in [Section 3](#) and in the analysis of wind speeds of tropical cyclones in [Section 4](#).

A fast inference method is extremely important for the modelling and analysis of datasets containing a large number of sites, especially when numerical procedures are required to work with an intractable form of the posterior distribution. Our method works with dense covariance matrices in the latent Gaussian processes, which scale poorly to large datasets due to the $\mathcal{O}(n^3)$ cost of covariance matrix inversions. In many applications, however, using a full covariance matrix may not be necessary. Indeed, computational complexity can be improved by either introducing sparsity in the covariance matrices or by reducing their dimensions. Methods that adopt the former approach typically involve assumptions about the dependence structure of the random effects, such as the SPDE approximation for the covariance matrix employed in the R-INLA implementation. An example of the latter approach is the inducing point method ([Quiñonero-Candela & Rasmussen, 2005](#); [Snelson & Ghahramani, 2006](#)) which has been widely used in Gaussian process regression with thousands of observations. [Titsias & Lawrence \(2010\)](#) have proposed a variational inference framework for dimension reduction for Gaussian process latent variable models, but this method only applies to models where both the likelihood and the prior are Gaussian. [Liu et al. \(2020\)](#) provide a recent review of Gaussian process methods which are scalable to large datasets. These methods in the Gaussian process literature are appealing from a theoretical point of view, but challenges remain in extending them to a general class of latent Gaussian process models with a non-Gaussian likelihood. Extending these methods to the GEV-GP setting is a promising direction for future work.

In this paper, we adopted a simple Taylor approximation for the conditional distribution of the random effects \mathbf{u} given the fixed parameters $\boldsymbol{\theta}$ of the GEV-GP model. [\(13\)](#), In a sense, we have assumed that it is sufficient to condition on the posterior mode of the fixed effects. This approach might result in relatively poor estimation of the random effects when the posterior distribution of the fixed effects is not log-convex or is multi-modal on the parameter space. Numerical quadrature techniques can potentially be used to integrate over multiple representative values of the fixed effects, resulting in a more accurate estimation of the posterior distribution of the random effects given $\boldsymbol{\theta}$. Applying such methods requires careful choice of the quadrature nodes and weights and other computational considerations. [Stringer \(2021\)](#) has implemented an adaptive Gauss-Hermite quadrature technique on a flexible class of latent Gaussian models. It is of interest to investigate its applicability to the GEV-GP model.

Acknowledgements

This work was supported by the Natural Sciences and Engineering Research Council of Canada, grant numbers RGPIN-2018-04376 (Ramezan), DGEER-2018-00349 (Ramezan) and RGPIN-2020-04364 (Lysy).

Declaration of Interest

None.

References

- Besag, J. (1974). Spatial interaction and the statistical analysis of lattice systems (with discussion). *Journal of the Royal Statistical Society. Series B (Statistical Methodology)*, *36*, 192–236.
- Besag, J., York, J., & Mollié, A. (1991). Bayesian image restoration with applications in spatial statistics (with discussion). *Annals of the Institute of Statistical Mathematics*, *43*, 19–59.
- Blanchet, J., & Davison, A. C. (2011). Spatial modelling of extreme snow depth. *Annals of Applied Statistics*, *5*, 1699–1725.
- Casson, E., & Coles, S. (1999). Spatial regression models for extremes. *Extremes*, *1*, 449–468.
- Castro-Camilo, D., Huser, R., & Rue, H. (2019). A spliced gamma-generalized Pareto model for short-term extreme wind speed probabilistic forecasting. *Journal of Agricultural, Biological, and Environmental Statistics*, *24*, 517–534.
- Castro-Camilo, D., Mhalla, L., & Opitz, T. (2020). Bayesian space-time gap filling for inference on extreme hot-spots: an application to red sea surface temperatures. *Extremes*, .
- Chen, M., Lysy, M., & Ramezan, R. (2021). *SpatialGEV: Fit Spatial Generalized Extreme Value Models*. URL: <https://github.com/meixichen/SpatialGEV> r package version 0.0.0.9000.
- Coles, S., & Powell, E. (1996). Bayesian methods in extreme value modeling: A review and new developments. *International Statistical Review*, *64*, 119–136.
- Coles, S. G. (2001). *An Introduction to Statistical Modeling of Extreme Values*. Springer.
- Coles, S. G., & Casson, E. (1998). Extreme value modelling of hurricane wind speeds. *Structural Safety*, *20*, 283–296.
- Cooley, D., Nychka, D., & Naveau, P. (2007). Bayesian spatial modeling of extreme precipitation return levels. *Journal of the American Statistical Association*, *102*, 824–840.

- Cooley, D., & Sain, S. (2010). Spatial hierarchical modeling of precipitation extremes from a regional climate model. *Journal of Agricultural, Biological, and Environmental Statistics*, *15*, 381–402.
- Davison, A., Padoan, S. A., & Ribatet, M. (2012). Statistical modeling of spatial extremes. *Statistical Sciences*, *27*, 161–186.
- Duane, S., Kennedy, A. D., Pendleton, B. J., & Roweth, D. (1987). Hybrid monte carlo. *Physics Letters B*, *195*, 216–222.
- Dyrddal, A. V., Lenkoski, A., Thorarinsdottir, T. L., & Stordal, F. (2015). Bayesian hierarchical modeling of extreme hourly precipitation in norway. *Environmetrics*, *26*, 89–106.
- Embrechts, P., Klüppelberg, C., & Mikosch, T. (1997). *Modelling Extreme Events: for Insurance and Finance*. Springer.
- Fawcett, L., & Walshaw, D. (2006). A hierarchical model for extreme wind speeds. *Applied Statistics*, *55*, 631–646.
- García, J. A., Martín, J., Naranjo, L., & Acero, F. J. (2018). A bayesian hierarchical spatio-temporal model for extreme rainfall in Extremadura (Spain). *Hydrological Sciences Journal*, *63*, 878–894.
- Ghosh, S., & Mallick, B. K. (2011). A hierarchical bayesian spatio-temporal model for extreme precipitation events. *Environmetrics*, *22*, 192–204.
- Gilli, M., & Küllezi, E. (2006). An application of extreme value theory for measuring financial risk. *Computational Economics*, *27*, 1–23.
- Hoffman, M. D., & Gelman, A. (2014). The No-U-Turn sampler: Adaptively setting path lengths in Hamiltonian Monte Carlo. *Journal of Machine Learning Research*, *15*, 1593–1623.
- Knapp, K. R., Diamond, H. J., Kossin, J. P., Kruk, M. C., & Schreck, C. J. (2010). International Best Track Archive for Climate Stewardship (IBTrACS) project, version 4. doi:<https://doi.org/10.25921/82ty-9e16>.
- Kristensen, K., Nielsen, A., Berg, C. W., Skaug, H., & Bell, B. M. (2016). TMB: Automatic differentiation and Laplace approximation. *Journal of Statistical Software*, *70*, 1–21.
- Lindgren, F. K., & Rue, H. (2015). Bayesian spatial modelling with R-INLA. *Journal of Statistical Software*, *63*, 1–25.
- Lindgren, F. K., Rue, H., & Lindström, J. (2011). An explicit link between Gaussian fields and Gaussian markov random fields: The stochastic partial differential equation approach (with discussion). *Journal of the Royal Statistical Society. Series B (Statistical Methodology)*, *73*, 423–498.

- Liu, H., Ong, Y.-S., Shen, X., & Cai, J. (2020). When Gaussian process meets big data: A review of scalable GPs. In *IEEE transactions on neural networks and learning systems*.
- Neal, R. M. (2011). MCMC using Hamiltonian dynamics. In *The Handbook of Markov Chain Monte Carlo* chapter 5. Chapman & Hall / CRC Press.
- Opitz, T. (2017). Latent Gaussian modeling and INLA: A review with focus on space-time applications. *Journal of the French Statistical Society*, *158*, 62–85.
- Opitz, T., Huser, R., Bakka, H., & Rue, H. (2018). INLA goes extreme: Bayesian tail regression for the estimation of high spatio-temporal quantiles. *Extremes*, *21*, 441–462.
- Palutikof, J. P., Brabson, B. B., & Adcock, S. T. (1999). A review of methods to calculate extreme wind speeds. *Meteorological Applications*, *6*, 119–132.
- Quiñonero-Candela, J., & Rasmussen, C. E. (2005). A unifying view of sparse approximate Gaussian process regression. *Journal of Machine Learning Research*, *6*, 1939–1959.
- Reich, B. J., & Shaby, B. A. (2012). A hierarchical max-stable spatial model for extreme precipitation. *The Annals of Applied Statistics*, *6*, 1430–1451.
- Rue, H., Martino, S., & Chopin, N. (2009). Approximate bayesian inference for latent Gaussian models by using integrated nested laplace approximations. *Journal of the Royal Statistical Society. Series B (Statistical Methodology)*, *71*, 319–392.
- Rue, H., Riebler, A., Sørbye, S. H., Illian, J. B., Simpson, D. P., & Lindgren, F. K. (2017). Bayesian computing with INLA: A review. *Annual Review of Statistics and Its Application*, *4*, 395–421.
- Sang, H., & Gelfand, A. E. (2008). Hierarchical modeling for extreme values observed over space and time. *Environmental and Ecological Statistics*, *16*, 407–426.
- Sang, H., & Gelfand, A. E. (2010). Continuous spatial process models for spatial extreme values. *Journal of Agricultural, Biological, and Environmental Statistics*, *15*, 49–56.
- Schliep, E. M., Cooley, D., Sain, S., & Hoeting, J. (2010). A comparison study of extreme precipitation from six different regional climate models via spatial hierarchical modeling. *Extremes*, *13*, 219–239.
- Smith, R., & Naylor, J. (1987). A comparison of maximum likelihood and Bayesian estimators for the three parameter Weibull distribution. *Applied Statistics*, *36*, 358–369.
- Snelson, E., & Ghahramani, Z. (2006). Sparse gaussian processes using pseudo-inputs. In *Advances in Neural Information Processing Systems 18* (pp. 1257–1264). MIT Press.
- Stan Development Team (2019). Stan modeling language users guide and reference manual. Version 2.26. URL: <https://mc-stan.org>.

Stan Development Team (2020). RStan: the R interface to Stan. URL: <http://mc-stan.org/> r package version 2.21.2.

Stringer, A. (2021). Implementing approximate bayesian inference using adaptive quadrature: the aghq package. [arXiv:2101.04468](https://arxiv.org/abs/2101.04468).

Titsias, M. K., & Lawrence, N. D. (2010). Bayesian Gaussian process latent variable model. In *the 13th International Conference on Artificial Intelligence and Statistics* (pp. 844–851). volume 9.

Tye, M. R., & Cooley, D. (2015). A spatial model to examine rainfall extremes in colorado’s front range. *Journal of Hydrology*, 530, 15–23.

Vehtari, A., Gelman, A., Simpson, D., Carpenter, B., & Bükner, P. (2021). Rank-normalization, folding, and localization: An improved \hat{R} for assessing convergence of MCMC. *Bayesian Analysis*, -1, 1–28.

Appendix A. Bayesian Posterior Prediction at Unobserved Locations

Let y_* denote the unobserved wind speed and $\mathbf{u}_* = (a(\mathbf{x}_*), b(\mathbf{x}_*))$ be the random effect parameters at a new location \mathbf{x}_* . Recall that $\mathbf{u} = (\mathbf{a}, \mathbf{b})$ is the vector of random effects at the observed locations and $\boldsymbol{\theta}$ is the vector of fixed effects. The posterior predictive distribution at the new location is given by

$$\begin{aligned} p(y_* | \mathbf{y}) &= \int p(y_* | a(\mathbf{x}_*), b(\mathbf{x}_*), s) p(\mathbf{u}_*, \boldsymbol{\theta} | \mathbf{y}) d\mathbf{u}_* d\boldsymbol{\theta} \\ &= \int p(y_* | a(\mathbf{x}_*), b(\mathbf{x}_*), s) \left(\int p(\mathbf{u}_* | \mathbf{u}, \boldsymbol{\theta}) p(\mathbf{u}, \boldsymbol{\theta} | \mathbf{y}) d\mathbf{u} \right) d\mathbf{u}_* d\boldsymbol{\theta} \\ &= \int p(y_* | a(\mathbf{x}_*), b(\mathbf{x}_*), s) \left(\int p(a(\mathbf{x}_*) | \mathbf{u}, \boldsymbol{\theta}) p(b(\mathbf{x}_*) | \mathbf{u}, \boldsymbol{\theta}) p(\mathbf{u}, \boldsymbol{\theta} | \mathbf{y}) d\mathbf{u} \right) d\mathbf{u}_* d\boldsymbol{\theta} \\ &= \int p(y_* | a(\mathbf{x}_*), b(\mathbf{x}_*), s) \left(\int p(a(\mathbf{x}_*) | \mathbf{a}, \boldsymbol{\theta}) p(b(\mathbf{x}_*) | \mathbf{b}, \boldsymbol{\theta}) p(\mathbf{u}, \boldsymbol{\theta} | \mathbf{y}) d\mathbf{u} \right) d\mathbf{u}_* d\boldsymbol{\theta}. \end{aligned}$$

Note that assuming a Gaussian distribution on the location parameter \mathbf{a} , we have

$$\begin{bmatrix} a(\mathbf{x}_*) \\ \mathbf{a} \end{bmatrix} \sim \mathcal{N} \left(\begin{bmatrix} 0 \\ \mathbf{0} \end{bmatrix}, \begin{bmatrix} \sigma_a^2 & \mathbf{K}_\theta(\mathbf{x}_*, \mathbf{X}) \\ \mathbf{K}_\theta(\mathbf{X}, \mathbf{x}_*) & \mathbf{K}_\theta(\mathbf{X}, \mathbf{X}) \end{bmatrix} \right).$$

where $\mathbf{X} = (\mathbf{x}_1, \dots, \mathbf{x}_n)^T$ and $[\mathbf{K}_\theta(\mathbf{X}, \mathbf{X})]_{ij} = k(\mathbf{x}_i, \mathbf{x}'_j | \sigma^2, \lambda)$ using (2).

Hence, we can obtain $p(a(\mathbf{x}_*) | \mathbf{a}, \boldsymbol{\theta})$:

$$\begin{aligned} a(\mathbf{x}_*) | \mathbf{a}, \boldsymbol{\theta} &\sim \mathcal{N}(m_{\text{new}}(\mathbf{x}_*), \sigma_{\text{new}}(\mathbf{x}_*)) \\ \text{with } m_{\text{new}}(\mathbf{x}_*) &= \mathbf{K}_\theta(\mathbf{x}_*, \mathbf{X}) \mathbf{K}_\theta(\mathbf{X}, \mathbf{X})^{-1} \mathbf{a}, \\ \sigma_{\text{new}}(\mathbf{x}_*) &= \sigma_a^2 - \mathbf{K}_\theta(\mathbf{x}_*, \mathbf{X}) \mathbf{K}_\theta(\mathbf{X}, \mathbf{X})^{-1} \mathbf{K}_\theta(\mathbf{X}, \mathbf{x}_*). \end{aligned}$$

$p(b(\mathbf{x}_*) | \mathbf{b}, \boldsymbol{\theta})$ can be obtained in the similar way as above.

$p(y_* | \mathbf{y})$ can be approximated by approximating integrals via Riemann sums and performing a multi-stage sampling scheme as follows.

1. Sample $(\mathbf{a}^j, \mathbf{b}^j, \boldsymbol{\theta}^j)$ from $p(\mathbf{u}, \boldsymbol{\theta} \mid \mathbf{y})$, $j = 1, 2, \dots, m$.
2. For each $(\mathbf{a}^j, \mathbf{b}^j, \boldsymbol{\theta}^j)$, sample $a^j(\mathbf{x}_*)$ and $b^j(\mathbf{x}_*)$ from $p(a(\mathbf{x}_*) \mid \mathbf{a}^j, \boldsymbol{\theta}^j)$ and $p(b(\mathbf{x}_*) \mid \mathbf{b}^j, \boldsymbol{\theta}^j)$.
3. For each $(a^j(\mathbf{x}_*), b^j(\mathbf{x}_*), s^j)$, sample y_*^j from $p(y_* \mid a^j(\mathbf{x}_*), b^j(\mathbf{x}_*), s^j)$. We end up with m draws of y_* .
4. The posterior mean of y_* can be approximated by $\frac{1}{m} \sum_{j=1}^m y_*^j$, and $L(\mathbf{x}_*)$ and $U(\mathbf{x}_*)$ can be approximated by the corresponding sample quantiles.